Toward optical coherence tomography angiography-based biomarkers to assess the safety of peripheral nerve electrostimulation

Srikanth Vasudevan[1,4], **Jesse Vo**[1,2], **Benjamin Shafer**[1], **Ahhyun S Nam**[3], **Benjamin J Vakoc**[3], and **Daniel X Hammer**[1,4]

[1]Division of Biomedical Physics, Office of Science and Engineering Laboratories, Center for Devices and Radiological Health, U.S. Food and Drug Administration, Silver Spring, MD, United States of America

[2]Fischell Department of Bioengineering, University of Maryland, College Park, MD, United States of America

[3]Wellman Center for Photomedicine, Harvard Medical School and Massachusetts General Hospital, Boston, MA, United States of America

Abstract

Objective.—Peripheral nerves serve as a link between the central nervous system and its targets. Altering peripheral nerve activity through targeted electrical stimulation is being investigated as a therapy for modulating end organ function. To support rapid advancement in the field, novel approaches to predict and prevent nerve injury resulting from electrical stimulation must be developed to overcome the limitations of traditional histological methods. The present study aims to develop an optical imaging-based approach for real-time assessment of peripheral nerve injury associated with electrical stimulation.

Approach.—We developed an optical coherence tomography (OCT) angiography system and a 3D printed stimulating nerve stabilizer (sNS) to assess the real-time microvascular and blood flow changes associated with electrical stimulation of peripheral nerves. We then compared the microvascular changes with established nerve function analysis and immunohistochemistry to correlate changes with nerve injury.

Main results.—Electrical stimulation of peripheral nerves has a direct influence on vessel diameter and capillary flow. The stimulation used in this study did not alter motor function significantly, but a delayed onset of mechanical allodynia at lower thresholds was observed using a sensory function test. Immunohistochemical analysis pointed to an increased number of macrophages within nerve fascicles and axon sprouting potentially related to nerve injury.

[4]Author to whom any correspondence should be addressed. Srikanth.Vasudevan@fda.hhs.gov (S Vasudevan) and Daniel.Hammer@fda.hhs.gov (D X Hammer).

Significance.—This study is the first to demonstrate the ability to image peripheral nerve microvasculature changes during electrical stimulation. This expands the knowledge in the field and can be used to develop potential biomarkers to predict nerve injury resulting from electrical stimulation.

Keywords

peripheral nerve injury; neuromodulation; electrical stimulation; optical coherence tomography

Introduction

Peripheral nerves relay information between the central nervous system and its targets. Recording activity from these nerves can provide information on the physiological state of the innervated organ system, and by applying targeted stimulation to the nerves, modulation of end organ function can be achieved. For example, applying electrical stimulation to the vagus nerve is used for the treatment of epilepsy and depression [1, 2]. Numerous applications of nerve stimulation are currently under investigation, such as for the treatment of rheumatoid arthritis, type II diabetes, and polycystic ovary syndrome [3–6]. As the field advances to identify new nerve targets for therapy, the development of novel nerve health assessment techniques in lieu of traditional histology will be of great benefit. This is especially important as nerve injury can potentially diminish therapeutic benefits or even accelerate disease progression.

Injury to peripheral nerve axons resulting from electrical stimulation has been well documented [7, 8], but little is known about the effects of electrical stimulation on nerve microvasculature and flow. Peripheral nerves are supplied blood from intrinsic and extrinsic sources, which are important to nerve health and optimal function. The epineurium and connective tissues surrounding the nerves form the extrinsic nerve blood supply system, and receive blood from vessels in the neighboring parenchyma. The intrinsic system is comprised of epineurial vessels and microvasculature between and within nerve fascicles [9–12]. Blood flow inside the fascicles is highly regulated and is critical for the maintenance of endoneurial homeostasis [13]. Disruption of blood flow associated with stretch or compression injuries can impair nutrient supply and under certain conditions lead to nerve injury [14–16]. The vasoconstrictive effect of electrical stimulation to control hemorrhage has been reported [17], but investigation of electrical stimulation induced nerve microvascular changes as an indicator of nerve injury has yet to be explored.

Optical coherence tomography (OCT) is an imaging technique where the axial (i.e. depth) resolution depends on the bandwidth of the illumination source rather than the illumination optics. This allows micron-level axial resolution, depth sectioning capability, and cross-sectional imaging nearly comparable to histological approaches irrespective of the objective numerical aperture. OCT also has an advantage compared to other common imaging modalities in terms of access to the phase information of the interferometric signal upon which the reflectance or image intensity is derived. This has led to development of decorrelation-based intrinsic contrast angiographic approaches distinct from Doppler OCT, which are commonly called OCT angiography (OCT-A) [18, 19]. OCT and OCT-A are used

routinely in ophthalmology owing to the immediate optical access of retinal tissue but are less commonly found in neuroscience investigations compared to other modalities (e.g. two-photon microscopy).

In this study, we developed an OCT-A system to investigate real-time vascular and blood flow changes associated with the electrical stimulation of peripheral nerves. Cuff electrodes used clinically for nerve stimulation therapies are not sized correctly for our animal studies, among other compatibility issues with our application. In addition, OCT-A is extremely sensitive to motion artifact, particularly from animal respiration and heartbeat, but also from electrical stimulation. Therefore, we also developed a custom 3D printed nerve stabilization holder with integrated electrodes. The overall objective of the study was to explore the use of OCT-A to detect stimulation-induced changes in peripheral nerve microvascular diameter and blood flow. We hypothesize that a change in nerve microvascular dynamics in response to electrical stimulation can be identified with real-time OCT-A imaging. This optical imaging approach has the potential to become a sensitive predictive biomarker of subtle peripheral nerve injury for current and future neuromodulation applications.

Methods

Surgical procedure

The animal study reported herein was approved by the Institutional Animal Care and Use Committee (IACUC) at the US Food and Drug Administration, White Oak campus. Female Lewis rats (259 ± 57 g) were purchased from Charles River Laboratories International Inc., USA. All animals were acclimated for 5 d upon receipt and subjected to 12 h light and dark cycles. Individual housing was used before and after experimental procedures. Animals were randomly assigned into two groups: sham ($n = 6$) and treatment ($n = 6$). All experimental procedures for the sham and treatment groups were identical, except that electrical stimulation was not applied to the nerve for the sham group.

Animals were first anesthetized with 4% isoflurane (induction), followed by intraperitoneal administration of a ketamine (75 mg kg^{-1}) and dexmedetomidine (0.25 mg k^{-1}g) cocktail. After confirming loss of toe pinch reflex, 2–3 ml of warm sterile saline was injected subcutaneously to prevent dehydration. Body temperature under anesthesia was maintained using heating pads throughout the surgery and imaging session. The left hind limb was shaved and disinfected using alcohol and betadine solution to ensure sterility. Under a sterile surgical field, the sciatic nerve was exposed through a skin incision, followed by sharp muscle dissection [20, 21]. The two split ends of the biceps femoris muscle were retracted by tying 4–0 polypropylene suture (Oasis Inc., USA) to the surrounding muscle tissue to keep the nerve exposed during imaging. Once the nerve was identified, a ~12 mm long segment of the nerve close to the trifurcation region was carefully freed from the surrounding connective tissue using microsurgical techniques. Saline was added to the region to prevent nerve dehydration while the animal was transferred to the OCT imaging system. A booster dose of anesthesia cocktail (100 μl) was administered once during the entire imaging procedure. Upon completion of the experimental procedures, the incisions were gently rinsed with sterile saline, the muscles were sutured, and the skin incision was stapled. Antibiotic ointment was applied over the skin incision to prevent infection.

Meloxicam (2 mg kg^{-1}) and Gentamicin (8 mg kg^{-1}) were administered subcutaneously for pain and infection management respectively, followed by administration of Atipamezole (0.5 mg kg^{-1}) intraperitoneally as a reversal agent. After anesthesia reversal, 2–3 ml of warm saline was injected subcutaneously to aid with recovery. Meloxicam (1 mg kg^{-1}) was further administered on days 1 and 2 post-experiment for pain management. On day 15 after experimental procedures, animals were anesthetized by administering a ketamine and dexmedetomidine cocktail and prepared for surgery as described above. Sciatic nerves were carefully dissected and immersion fixed in 4% paraformaldehyde solution for immunohistochemical assessment. Finally, the animals were administered intraperitoneal pentobarbital (200 mg kg^{-1}) for euthanasia.

OCT system setup

A custom spectral domain OCT system was used to image the rat sciatic nerve as shown in figure 1(A) and described in detail elsewhere [18]. The system uses a 1310 nm (center wavelength) superluminescent diode light source (Exalos, Switzerland), a custom spectrometer (Wasatch Photonics Inc., USA), and a 76 kHz line rate InGaAs linear detector (Sensors Unlimited Inc., USA). The optics were modified from the previously reported configuration for a moderate lateral resolution and depth-of-focus (DOF) for imaging peripheral nerves. The source collimator (focal length = 19 mm) produces a beam diameter of ~3 mm and a 5× telecentric objective (LSM03, 25.1 mm working distance, Thorlabs Inc., USA) achieves a spot size of 11 μm and a DOF of ~800 μm, measured with a 3D point spread function phantom, roughly matching the light penetration depth in the highly-scattering rat sciatic nerve (approximate diameter ≈ 1.2–1.5 mm). Angiography from the acquired images was performed using amplitude decorrelation, by computing the mean absolute difference between B-scans sets from each lateral position [19]. Capillary flowmetry is also performed using an algorithm based upon Srinivasan *et al* [22]. The gate-length (*M*), the total number of B-scans obtained for the angiography and flowmetry calculation, was set to 10 or 100 (see below). Image acquisition and processing of reflectance, angiography, and capillary flowmetry images was performed in real-time using custom CUDA-based code running on the system graphics processing unit (GPU).

Nerve stabilizer design and fabrication

Suppression of motion artifacts resulting from respiration, heartbeat, and electrical stimulation was achieved using a custom 3D printed nerve stabilizer. A 3D model was created using SolidWorks (Dassault Systèmes SolidWorks Corporation, USA) and printed with a Connex3 Objet260 printer (Stratasys, USA). A detailed schematic of the sNS with dimensions is shown in figure 1 (D). The material used to print the sNS (Vero White plus PolyJet Material) provided rigidity for stabilizing the nerve from respiratory and stimulation-induced body motion. A hemi-cuff electrode was designed with two stimulation electrodes placed inside the nerve channel and one ground electrode on the backside of the nerve stabilizer (Microprobes for Life Science, USA). Polyimide coated platinum/Iridium wires (0.05 mm diameter) were used to make stimulating (0.4 mm deinsulation) and ground electrodes (20 mm deinsulation). Figure 1(B) shows the stimulating nerve stabilizer (sNS) used in this study. The sNS was fixed to the motorized animal stage to provide stability during imaging (figure 1(C)).

Electrical stimulation parameters

In the treatment group, nerve stimulation was applied using a constant current source (Keithley Instruments, Tektronix, Inc., USA) controlled with a custom MATLAB script. Stimulation to the nerve was applied using a waveform modified from the one described by Agnew and colleagues [23]. A cathodic first charge balanced square waveform with 100 μs pulse width, 5 mA amplitude, and 400 μs interphase delay at 50 Hz was applied for 1 h. The stimulation produces a charge density of 748.96 μC/cm^2/phase with a Shannon k value of 2.57 [24], which is expected to produce injury to the nerves, based upon previous studies in peripheral nerves [7, 8, 23].

Imaging-stimulation protocol

The animal was placed on a computer-controlled motorized stage with the left sciatic nerve facing the objective. A single 1.5 × 7.5 mm (250 × 1250 pixels, not including fly-back) angiography scan ($M = 10$), with the long axis along the nerve length, was acquired before the nerve was positioned in the sNS (i.e. native state) to aid with nerve alignment. The sNS was carefully positioned under the nerve to minimize stretching and tension. Nerve proximity to the stimulating electrode was confirmed using fast OCT raster scans. During the hour-long stimulation, nerve hydration was maintained by placing a piece of plastic wrap (Saranwrap, Saran, USA) over the nerve and with regular administration of warm sterile saline. A total of 6 scans (1.5 × 7.5 mm, $M = 100$) were acquired with the nerve in sNS, as shown in figure 2. Each scan took ~16 min to complete. After the six angiography/flow scans, the sNS was removed and a final native state scan ($M = 10$) was acquired. All aspects of the experimental protocol (e.g. surgery, nerve placement in sNS in contact with electrodes, imaging scans) were identical for the sham animals, except that the electrodes were not connected to the stimulator. Scan start time in sham group was matched to the treatment group for comparison. After completion of experimental procedures, the wound was closed and the animals recovered as described in the surgical procedure section above. A detailed schematic representation of the experimental protocol is shown in figure 2.

Angiography and flow analysis

Vessel diameter and peak flow measurements were calculated on *en-face* images created from the volumetric OCT data sets. *Z*-projections 0.8 mm thick (200 pixels), approximately the thickness of the light penetration depth into the nerve, were created using average intensity projection (AIP) for reflectance and angiography sets, and maximum intensity projection (MIP) for the flow set. *En-face* images for each animal at each timepoint were registered using StackReg in ImageJ (Fiji) or custom registration software. Custom software was written to manually size and measure peak flow in the vessels. Small regions-of-interest (10 pixels wide) were chosen over each vessel segment to be analyzed, where the region was manually rotated until perpendicular to the vessel. Once robust vessel diameter measurement was verified for all time points, the full-width half-maximum (FWHM) vessel diameter was calculated. Vessel segments were chosen between branch points or with spacing of at least a few hundred micrometers. Once the regions were chosen and applied to each angiography map, the same regions were transferred to the identically registered MIP flow maps, where the peak flow velocity (mm/s) in each vessel was extracted and calculated. The vessel

diameter and flow values were normalized to baseline. The total number of vessel diameter measurements from all animals was $n = 84$ for the sham animals and $n = 82$ for the treatment animals. The total number of capillary flow measurements from all animals was $n = 82$ for the sham animals and $n = 81$ for the treatment animals. For each measurement, values were normalized to baseline for comparison. Data within (sham and treatment) groups were compared using two-way ANOVA (Prism 6, GraphPad Software, USA) followed by Tukey's multiple comparison test and between group timepoints were compared using two-way ANOVA followed by Bonferroni's multiple comparison test.

We also compared two machine learning algorithms, support vector machine (SVM) and logistic regression (LR) using Orange 3.18.0 software package [25], to evaluate their respective classification accuracy to distinguish the sham and treatment groups. We set the sham and treatment labels as the target, with S1, S2, S3, R1, and R2 as the features. Data used for training and testing were normalized to baseline. We compared the classification accuracy between SVM and LR using only vessel diameter data (166 instances, five features), only capillary flow data (163 instances, five features), and combination of vessel diameter and capillary flow data (163 instances, ten features). Training set size was set to 90%, with random sampling. Training and testing was repeated ten times to compute the average classification accuracy as shown in figure 7(E).

Assessment of nerve function

Nerve injury induced changes to motor and sensory function were assessed with walking track analysis and Von Frey test respectively, as described elsewhere [20]. Nerve function was assessed before experimental procedures for baseline (pre-stimulation) and at one-week and two-weeks post experimental procedures to determine functional deficits and recovery.

To perform motor function assessment using walking track analysis, animals were placed on a plexiglass platform (FreeWalk, Cleversys Inc., USA), confined within an 8×40 cm region. High resolution videos were recorded from beneath the platform for further analysis of five consecutive full steps. Videos were imported into ImageJ for frame-by-frame measurements of the left foot print length (LPL), toe spread (LTS), and intermediary toe spread (LITS), along with the measurement of right foot print length (RPL), toe spread (RTS), and intermediary toe spread (RITS). The sciatic function index (SFI) and tibial function index (TFI) were calculated using equations (1) and (2) [26]. The average of 5 SFI and TFI values from each session was used for data analysis.

$$\text{SFI} = -38.3\left(\frac{\text{LPL}-\text{RPL}}{\text{RPL}}\right) + 109.5\left(\frac{\text{LTS}-\text{RTS}}{\text{RTS}}\right) + 13.3\left(\frac{\text{LITS}-\text{RITS}}{\text{RITS}}\right) - 8.8 \quad (1)$$

$$\text{TFI} = -37.2\left(\frac{\text{LPL}-\text{RPL}}{\text{RPL}}\right) + 104.4\left(\frac{\text{LTS}-\text{RTS}}{\text{RTS}}\right) + 45.6\left(\frac{\text{LITS}-\text{RITS}}{\text{RITS}}\right) - 8.8. \quad (2)$$

To assess changes to sensory function, hind paw withdrawal thresholds were measured using the Von Frey test. Animals were placed inside a custom 25.4×25.4 cm cage with a

perforated floor. Animals were allowed 5 min for acclimation before measurements were taken. Rigid filament of the electronic anesthesiometer (IITC Life Science Inc., USA) was pressed against the central region of the left foot plantar surface. Five trials of complete foot withdrawal (mechanical allodynia) per session were recorded, and the average value was used for data analysis.

Data within group were compared using two-way ANOVA (Prism 6, GraphPad Software, USA) followed by Tukey's multiple comparison test and between group timepoints were compared using two-way ANOVA followed by Bonferroni's multiple comparison test.

Immunohistochemical assessment

Sciatic nerve regions from the experimental hind limb that was placed inside the sNS nerve channel were harvested and immersion fixed in 4% paraformaldehyde solution at 4 °C for immunohistochemical processing. Control sciatic nerves were obtained from the contralateral hind limb of the sham group for comparison. Fixed tissues were rinsed with phosphate buffered saline (PBS), embedded in paraffin (ASP300 S, Leica Biosystems, Germany) and sliced to obtain ~10 μm sections. Sections were de-paraffinized and processed for immunohistochemistry as described in detail elsewhere [20]. Sections were incubated in blocking solution made with PBS solution containing 4% goat serum (Thermo Fisher Scientific, USA) and 0.5% Triton X-100 (Sigma Aldrich, USA), at room temperature for 1 h. Sections were incubated overnight at 4 °C in blocking solution containing primary antibodies against macrophages for the detection of CD68 (mIgG1, EMD Millipore, USA) and β-Tubulin (RbIgG, Sigma Aldrich, USA) for axons. After thoroughly washing with PBS solution containing 0.5% Triton X-100, sections were incubated in washing solution containing secondary antibodies to detect macrophages (GamIgG1, Jackson Immuno Research, USA) and axons (GamRbIgG, Jackson Immuno Research, USA). Finally, samples were rinsed in washing solution and counterstained with DAPI (Life Technologies, USA). Fluorescent images (Zeiss, Germany) of six fields from each nerve sample were acquired with a 20× objective. Images of macrophages and axons were quantified using ImageJ. A region of interest (ROI) was drawn to include nerve fascicles identified by β-Tubulin and the total number of macrophages were counted and normalized to 1 Mpx^2 of the ROI. To count axon pixels, images were converted to 8-bit and Huang's auto-thresholding method was implemented. Manual threshold input was used when auto-thresholding did not produce optimal coverage of axons. Pixels corresponding to axons were counted and normalized to 1 Mpx^2 of the ROI. One-way ANOVA followed by Tukey's test (Prism 6, GraphPad Software, USA) was used for data comparison.

Results

Surgical procedure

Imaging exposed nerves under anesthesia for several hours requires optimization of anesthetic dosage, a strategy to maintain hydration, and a plan for successful animal recovery after the experiments. In this study, we administered an anesthesia cocktail before imaging and once during imaging to maintain optimum levels of anesthesia throughout the ~4 h long experimental session. Administration of warm saline via subcutaneous injection

before and after the experimental procedure prevented dehydration and aided with post-procedural recovery. Administration of analgesics and antibiotics prevented adverse events such as animal distress, pain, and infection. Prevention of adverse events was critical to successfully administer post-experimental functional assays and histological procedures. In this study, our optimized surgical procedure was proven conducive to the development of optical imaging-based biomarkers of nerve injury, because no adverse events occurred.

Nerve stabilization for imaging

Isolation and stabilization of the sciatic nerve from surrounding muscles is critical to suppress respiratory-related motion artifacts that can corrupt OCT-A images. When electrical stimulation is applied to the nerve, rapid muscle contractions induce motion artifacts leading to poor quality OCT-A images. The 3D printed sNS device used in this study served two main purposes: (1) to isolate and suppress motion artifacts and (2) to align in three dimensions a segment of the sciatic nerve inside the channel for imaging. To illustrate the benefit of the sNS, figure 3 shows OCT *en-face* AIP images taken without (i.e. the initial native state scan) and with the nerve stabilizer without stimulation. The horizontal lines in the native state images (figures 3(A) and (C)) are predominantly caused by respiratory motion while the images taken with the sNS in place (figures 3(B) and (D)) are generally free of motion artifact. The finest capillaries can be resolved when motion is controlled in this manner. Imaging during stimulation was generally achieved without additional motion artifacts. Also note the lateral and axial alignment of the nerve in the image with sNS, where the nerve is straight and in focus along the entire length of the 5 mm channel. In contrast, the nerve in the native image moves out of focus at the end of the image as the OCT beam scans over the anatomical topography of the animal's leg. Additionally, it can be seen from the vessel pattern that there can be some torsional displacement (i.e. rolling along the nerve axis) as the nerve is positioned in the sNS. Care was taken during sNS placement to prevent nerve stretching, which could affect flow in the blood vessels. The nerve was positioned adjacent to and in contact with the stimulating electrodes and confirmed from the OCT reflectance image (see figure 4(D)) prior to stimulation. The Saranwrap was placed over the nerve at an angle (figure 4(B)), which prevented dehydration and eliminated image corruption by specular reflection from the top of the nerve.

OCT imaging and analysis

The optics of the OCT-A system used in this study were designed to achieve a moderate DOF to access structures, particularly deeper vessels, within peripheral nerve fascicles. Figure 4 shows example reflectance, angiography, and flow cross-sectional (CS) and *en-face* (EF) views of the rat sciatic nerve. The CS views were produced by summing 25 frames (0.15 mm) at three different regions delineated by the dashed regions in the EF view (200-frame AIP). The EF reflectance image (figure 4(D)) shows good apposition between the nerve and electrodes. The CS reflectance images (figures 4(A)–(C)) show light penetration to ~50%–75% of the highly scattering nerve, as expected. The Saranwrap, epineurium, and fascicles can be easily identified in the CS OCT reflectance images, as well as anatomically important structures, such as nerve separating into three and four distinct fascicles. The CS angiography images (figures 4(E) and (F)) show the axial position of the microvasculature in the epineurium and inside individual fascicles. The EF angiography image (figure 4(H))

shows interaction between the extrinsic and intrinsic blood supply systems, critical for maintaining nerve homeostasis. The CS flow images of the corresponding vessels (figures 4(E)–(G)) show a difference in flow rate between the epineurial and endoneurial vasculature. The EF flow image (figure 4(L)) shows a higher flow rate in the larger vessels traversing the nerve surface compared to the deeper vessels within the nerve, however, this may have to do with light scatter and penetration and requires further investigation. OCT-A is thus a promising method to study physiological changes associated with peripheral nerve microvasculature in response to electrical or other forms of stimulation.

Vascular flow was calibrated using a uniform scattering phantom (Spectralon, Labsphere Inc., North Sutton, New Hampshire) on a precision linear stage moving at constant velocity similar to that described previously for a different configuration of the same OCT imager [27]. Figure 5 shows the calibration results. The flow algorithm produces a frequency bandwidth (f) that is linearly proportional to velocity within a window bound by system noise on the low end and decorrelation saturation on the high end. Between those bounds is the operable range for a particular configuration of system optics (i.e. beam spot size) and scan dimensions, spacing (or density), and timing (i.e. beam overlap). Calibration was performed by moving the stage at fixed velocities while imaging the uniform scattering phantom with identical scan parameters as those used in the animal study. At each velocity, the mean f is calculated in a 50×200 pixel ROI within the phantom (figure 5(B)). Once a linear least squares fit was found between f and velocity, the flow images could be directly and accurately converted to velocity via the linear relationship. Owing to decorrelation saturation, peak flow values above the operable velocity range (~3.5–4 mm s^{-1}) will underestimate vascular flow. Underestimation of peak flow will also occur if values above the operable range are removed since we know the actual flow value is above the value calculated with calibration. The calibration curve in figure 5 indicates that the maximum inaccuracy up to a measured flow velocity of 4 mm s^{-1} is 8%.

Figure 6 shows a portion of the sciatic nerve for one treatment animal for the duration of the experiment. The panels in figures 6(B) and (C) are for baseline, stimulation (S1, S2, S3), and recovery (R1, R2). Figure 6(D) shows vessel profiles measured at a single region over the course of the experimental protocol. Absolute quantification of vessel diameter and flow rate are shown in figures 6(E) and (F). The vasodilation and increase in flow velocity with stimulation are apparent. While both vessel diameter and flow leveled off, the total recovery duration (45 min) was not sufficient for values to return to baseline. Permanent damage may also have prevented full recovery.

Vessel diameter (FWHM) comparisons between the sham and treatment groups are shown in figures 7(A) and (B). The vessel diameter in the sham group varied little from baseline, indicating good control of experimental variability. On the other hand, the treatment group showed continuously increasing dilation throughout stimulation (9% to 24%) and even after stimulation cessation as shown in figure 7(A). The vessel diameters between sham and treatment groups were significantly different during timepoints S1, S3, R1, and R2 as shown in figure 7(B). The vessel diameter changes in the treatment group indicate a direct effect of electrical stimulation on nerve vasculature.

Capillary flow was measured from the same vessels of the sham and treatment groups and is shown in figures 7(C) and (D). As with the vessel diameter measurement, the sham group showed no significant difference from baseline for flow. The treatment group showed a significant immediate increase in flow of 20% after stimulation onset, which continued through timepoint R2. The sham and treatment groups were significantly different at all timepoints as shown in figure 7(D). This difference between the sham and treatment groups indicates the underlying effects of electrical stimulation on nerve blood flow.

The classification accuracy of both SVM and LR algorithms show improvement when both vessel diameter and flow information are used together as features. The LR algorithm was slightly better than SVM, with classification accuracy of 75.9% and 72.4% respectively, when both vessel diameter and flow data are used together. The confusion matrix in figure 7(E) shows the prediction accuracy of the LR algorithm, with better detection for sham over treatment group. Overall, the outcomes of these algorithms point to an underlying difference between sham and treatment groups, once again indicating the effects of electrical stimulation on both vessel diameter and flow.

Assessment of nerve function

The change in motor function in response to the experiments was assessed using walking track analysis (figure 8(A)). In both sham and treatment groups, no significant functional deficits were observed at weeks 1 and 2 compared to pre-stimulation values. Change in sensory function was assessed using the Von Frey test (figure 8(B)). While the sham group did not exhibit a difference at weeks 1 and 2 compared to pre-stimulation baseline, there was a delayed alteration in sensory function in the treatment group at two weeks compared to pre-stimulation. This significant change in mechanical allodynia (hypersensitivity) can potentially be a result of electrical stimulation induced nerve injury.

Immunohistochemical assessment

Immune response to nerve injury was assessed using macrophage staining as shown in figure 9. The presence of macrophages and blood vessels inside the nerve fascicle can be seen in figure 9(A). Baseline levels of CD68+ cells were observed in control nerves (contralateral nerves extracted from the sham group), while an increased level was observed in both sham and treatment groups indicating nerve injury resulting from the experimental setup. However, only the treatment group was significantly different from the control group, pointing to the direct effects of electrical stimulation on nerve injury. Axon counts were assessed using β-Tubulin staining as shown in figure 9(D). Even though there was no significant difference between groups, the treatment group points to higher number of axons, which could be attributed to an increase in axon sprouting from fibers regenerating after injury.

Discussion

Modulating peripheral nerve activity through targeted stimulation, known as neuromodulation, is currently being studied for numerous therapeutic applications. Some examples of emerging neuromodulation therapies include inflammatory bowel disease,

rheumatoid arthritis, type II diabetes, and polycystic ovary syndrome [3–6, 28, 29]. Stimulating residual peripheral nerves has also been used to restore sensory function in amputees for neural interface applications [30–32]. To augment the benefits from peripheral nerve stimulation, parameter optimization studies have also been conducted [33, 34]. However, to maximize positive outcomes from peripheral nerve stimulation-based approaches, it is critical to prevent nerve injury resulting from the electrical stimulation itself. Continuous electrical stimulation of peripheral nerves has been shown to induce nerve damage [8, 35], which can potentially render the therapy ineffective, or even worsen disease progression. Assessment of nerve injury is traditionally performed using end-point histology [23, 35], which provides quantitative information regarding the extent of nerve damage. For histological assessment, one needs to allow sufficient time for the injury to manifest. Therefore, assessment methods that can be used to predict and prevent nerve injury in real-time can significantly improve outcomes of peripheral nerve electrical stimulation therapies. In this work, we developed an OCT-A based technique to image peripheral nerves and applied it to study vascular dynamics during electrical stimulation. The vascular metrics have the potential to serve as sensitive biomarkers of electrostimulation induced nerve injury.

In vivo imaging of the sciatic nerve in rats using OCT can be challenging, as it is affected by respiratory artifacts [36] (see figure 3). When electrical stimulation above the activation threshold is applied to the sciatic nerve, it leads to rapid muscle contractions [37]. Because OCT-A detects flow from changes in the spatial speckle pattern, tissue motion will lead to signal in the angiograms. If the nerve is not stabilized during muscle contractions, the OCT-A images are completely saturated with artifacts, rendering the images unusable for analysis. While stabilization of the nerve is critical for imaging, limiting nerve stretch from the experimental procedures is equally important to prevent nerve injury. The exposed rat sciatic nerve exhibits a wave-like structure known as bands of Fontana, which diminishes as the nerve undergoes extensive stretching [38, 39]. To perform OCT imaging during electrical nerve stimulation, without subjecting the nerve to extensive stretching, we developed a 3D printed sNS with embedded stimulation electrodes (figure 1(B)). A segment of the nerve is aligned within the nerve channel of the sNS, which is then attached to the 3-axis stage for stability (figure 1(C)). From the reflectance images (red arrow, figure 4(D)), we can observe the characteristic bands of Fontana indicating that neither our surgical procedures nor placement in the sNS produced extensive nerve stretching. Stability of the nerve during stimulation is confirmed by the presence of discernable angiography and flow data (figures 4(H) and (L)), which eliminates the need to use extensive post-processing motion correction algorithms.

Assessment of peripheral nerve injury involves the analysis of axons and other components in the region distal to the site of injury [40]. A comprehensive method of nerve analysis requires tissue fixation, and cannot capture events as they occur in real-time. While nerve injury takes time to manifest in the distal nerve segment, sensitive biomarkers may provide earlier direct evidence of damage or indications that can be used to predict nerve injury. One potential target is peripheral nerve microvasculature, which plays an important role in maintaining the nutrient supply within the nerve [41]. The role of microvasculature in traumatic peripheral nerve injury induced neuropathic pain in rodent models involves

endoneurial hypoxia [42]. In this study, we found evidence of immediate vasodilation in the treatment group during electrical stimulation and after stimulation cessation (figures 7(A) and (B)). This may indicate some level increase in metabolic demand and a direct effect of electrical stimulation on nerve microvasculature. In the treatment group, we also found that the microvascular flow increases upon stimulation and tends to remain at higher levels compared to baseline even after stimulation cessation (figures 7(C) and (D)). Previous studies also show that injury to peripheral nerves can lead to an increase in nerve blood flow [41]. While the increase in blood flow in the treatment group could point to electrical stimulation induced nerve injury, the gradual decrease in flow in the sham group could be related to reduced metabolic needs of an animal under anesthesia in the resting state.

Injury to peripheral nerves can lead to loss of motor function, which can be tracked by examining footprints using walking track analysis [26, 43]. In this study, we observed that the sham group showed relative stability of motor function one and two weeks after experimental procedures, while the treatment group SFI and TFI showed a slight decrease at one week followed by recovery of function at two weeks (figure 8(A)). This change in function may indicate some impact of electrical stimulation on motor function, and most importantly, points to the lack of sensitivity of walking track analysis to detect subtle nerve injuries. It is also important to note that the experimental setup and stimulation did not impede recovery of motor function, which is critical to avoid confounds. On the other hand, sensory function assessment using Von Frey test [44] showed a significant change in the treatment group at two weeks, pointing to an electrical stimulation induced reduction in threshold for mechanical allodynia (figure 8(B)). Overall, the delayed onset of pain hypersensitivity may be ascribed to nerve injury resulting from electrical stimulation in the treatment group. Additional investigation using different stimulation parameters and further imaging (e.g. at the two week time point when the nerve is re-exposed for histological assessment) could provide additional evidence to understand overstimulation effects.

Immunohistochemical assessment of nerves allowed visualization of axons, macrophages and blood vessels within the nerves (figures 9(A)–(C)). The number of macrophages was significantly higher in the treatment group compared to control (figure 9(D)). The increased number of macrophages can be attributed to electrical stimulation induced nerve injury in the treatment group, as macrophage infiltration is associated with Wallerian degeneration [45]. The total number of axon pixels in the treatment group is 17.1%, 9.3% higher than the control and sham groups, which could indicate axonal damage induced sprouting (figure 9(D)) or anatomical variability (size and number of axons). An increase in number of axons (sprouting) has been associated with nerve regeneration [45].

There are several limitations in the current study that should be considered with the results. First, anesthesia is a known confounding influence on blood flow measurements. Second, the vascular anatomy in the sciatic nerve differs between animals. Some of the vessels used for quantification were closer to the stimulating electrodes compared to others. Third, while the number of animals used in this study is sufficient to detect nerve injury using histology [46], more animals may be required to ascertain optical imaging based predictive biomarkers of nerve injury. Fourth, we used only one stimulation parameter to induce nerve injury in the treatment group for this proof-of-principle study. We expected to observe nerve injury since

the charge and charge density per phase leads to a Shannon k value of 2.57, and the frequency of 50 Hz stimulation is known to cause early axon degeneration during continuous nerve stimulation [7, 8, 23, 24, 35]. Since we wanted to include nerve function tests along with immunohistochemical assessment, we were not able to harvest the nerve around 7 d post-stimulation to assess nerve injury. Also, as described in the methods, the absolute flow values are likely a slight underestimation of the actual values. None of the measured peak flow values exceeded 4.5 mm s^{-1}. We chose to use peak values, rather than mean or median values, as a representation of the maximum flow in any individual vessels, including larger vessels that may have laminar (i.e. parabolic) flow profiles across the vessel. Excluding flow pixels above 4 mm s^{-1} or using mean values with or without pixels outside of the linear range will not remove this underestimation. We also combined results from capillaries with larger vessels, where larger vessels are regulated by neural signals [47]. We tried to mitigate these limitations in the flow measurements by using normalized values and only interpreting coarse trends with stimulation. This may answer the question of whether electrical stimulation affects vessel diameter and flow but more investigation is required to determine how this occurs.

Optical-based assessment of overstimulation or nerve damage is a relatively unexplored application of optical imaging [36], which suffers from light penetration loss from tissue scattering that prevents direct transcutaenous visualization of most nerves; the retinal nerve fiber layer being one exception (accessed intraocularly). All *in vivo* imaging applications also must contend with motion, which as we have shown, is particularly corrupting for OCT-A. While the challenge of light penetration, exposed nerve access, and motion will need to be overcome to use optical imaging for *in vivo* peripheral nerve applications, technological progress points to several potential areas where this tool may add value. First, one can envision incorporating OCT modalities for surgical guidance to identify nerves intraoperatively [48], This can potentially identify nerves and plexus without the use of contrast agents for peripheral neuromodulation applications. For applications involving implants, such as nerve cuff electrodes, OCT can be used in real-time to prevent mechanical trauma or overstimulation. This can serve as a powerful tool to improve both safety and efficacy of the intended neuromodulation therapy. Second, one could envision optical imaging integrated into implanted stimulators like the vagus nerve stimulator. This would require considerable progress towards miniaturization over what exists today. However, some miniaturization of optical hardware has already been achieved for other applications. One example is the OCT tethered capsule endomicroscope for Barrett's esophagus and other conditions of the gastro-intestinal tract [49]. Another example where significant engineering has been achieved is the small animal mounted optical microscopes for functional cortical imaging [50]. These examples illustrate the potential for future extension of OCT-A and other OCT variants (polarization-sensitive OCT) in the peripheral nerve domain, particularly in terms of device safety assessment.

Conclusion

We developed an approach, using optical angiography of stabilized nerves, to assess the effect of electrical stimulation on nerve microvasculature and flow. We observed vasodilation and increase in blood flow upon electrical stimulation. The results indicate the

experimental setup did not produce significant loss of function, providing a reliable method of nerve injury assessment. Motor function testing indicated no significant loss, while a delayed sensory hypersensitivity may have been caused by electrical stimulation, which was supported by immunohistochemical assessment. The challenge remains to detect stimulation damage very near threshold when the time-course of injury is delayed. Optical imaging-based approaches and the measures derived from them may be useful tools to apply to this challenge. Further investigation is required to continue to develop optical imaging based, sensitive, and predictive biomarker of subtle peripheral nerve injury for current and future neuromodulation applications.

Acknowledgments

References

[1]. Johnson RL and Wilson CG 2018 A review of vagus nerve stimulation as a therapeutic intervention J. Inflamm. Res 11 203–13 [PubMed: 29844694]

[2]. Yuan H and Silberstein SD 2016 Vagus nerve and vagus nerve stimulation, a comprehensive review: part III Headache 56 479–90 [PubMed: 26364805]

[3]. Famm K, Litt B, Tracey KJ, Boyden ES and Slaoui M 2013 Drug discovery: a jump-start for electroceuticals Nature 496 159–61 [PubMed: 23579662]

[4]. Koopman FA et al. 2016 Vagus nerve stimulation inhibits cytokine production and attenuates disease severity in rheumatoid arthritis Proc. Natl Acad. Sci. USA 113 8284–9 [PubMed: 27382171]

[5]. Sacramento JF et al. 2018 Bioelectronic modulation of carotid sinus nerve activity in the rat: a potential therapeutic approach for type 2 diabetes Diabetologia 61 700–10 [PubMed: 29332196]

[6]. Pikov V, Sridhar A and Lara HE 2018 High-frequency electrical modulation of the superior ovarian nerve as a treatment of polycystic ovary syndrome in the rat Frontiers Physiol 9 459

[7]. Agnew WF, McCreery DB, Yuen TG and Bullara LA 1990 Local anaesthetic block protects against electrically-induced damage in peripheral nerve J. Biomed. Eng 12 301–8 [PubMed: 2395356]

[8]. McCreery DB, Agnew WF, Yuen TG and Bullara LA 1995 Relationship between stimulus amplitude, stimulus frequency and neural damage during electrical stimulation of sciatic nerve of cat Med. Biol. Eng. Comput 33 426–9 [PubMed: 7666690]

[9]. Beggs J, Johnson PC, Olafsen A, Watkins CJ and Cleary C 1991 Transperineurial arterioles in human sural nerve J. Neuropathol. Exp. Neurol 50 704–18 [PubMed: 1748879]

[10]. Gao Y, Weng C and Wang X 2013 Changes in nerve microcirculation following peripheral nerve compression Neural Regen. Res 8 1041–7 [PubMed: 25206398]

[11]. Ubogu EE 2013 The molecular and biophysical characterization of the human blood-nerve barrier: current concepts J. Vasc. Res 50 289–303 [PubMed: 23839247]

[12]. Zamir M, Twynstra J, Vercnocke AJ, Welch I, Jorgensen SM, Ritman EL, Holdsworth DW and Shoemaker JK 2012 Intrinsic microvasculature of the sciatic nerve in the rat J. Peripher. Nervous Syst 17 377–84

[13]. Mizisin AP and Weerasuriya A 2011 Homeostatic regulation of the endoneurial microenvironment during development, aging and in response to trauma, disease and toxic insult Acta Neuropathol 121 291–312 [PubMed: 21136068]

[14]. Tyler DJ and Durand DM 2003 Chronic response of the rat sciatic nerve to the flat interface nerve electrode Ann. Biomed. Eng 31 633–42 [PubMed: 12797612]

[15]. Lundborg G and Rydevik B 1973 Effects of stretching the tibial nerve of the rabbit. A preliminary study of the intraneural circulation and the barrier function of the perineurium J. Bone Joint Surg. Br 55 390–401 [PubMed: 4707307]

[16]. Ogata K and Naito M 1986 Blood flow of peripheral nerve effects of dissection, stretching and compression J. Hand Surg. Br 11 10–4 [PubMed: 3958526]

[17]. Mandel Y, Manivanh R, Dalal R, Huie P, Wang J, Brinton M and Palanker D 2013 Vasoconstriction by electrical stimulation: new approach to control of non-compressible hemorrhage Sci. Rep 3 2111 [PubMed: 23828130]

[18]. Hammer DX, Lozzi A, Abliz E, Greenbaum N, Agrawal A, Krauthamer V and Welle CG 2014 Longitudinal vascular dynamics following cranial window and electrode implantation measured with speckle variance optical coherence angiography Biomed. Opt. Express 5 2823–36 [PubMed: 25136505]

[19]. Lozzi A, Agrawal A, Boretsky A, Welle CG and Hammer DX 2015 Image quality metrics for optical coherence angiography Biomed. Opt. Express 6 2435–47 [PubMed: 26203372]

[20]. Vasudevan S, Patel K and Welle C 2017 Rodent model for assessing the long term safety and performance of peripheral nerve recording electrodes J. Neural Eng 14 016008 [PubMed: 27934777]

[21]. Vasudevan S, Yan JG, Zhang LL, Matloub HS and Cheng JJ 2013 A rat model for long-gap peripheral nerve reconstruction Plast. Reconstr. Surg 132 871–6 [PubMed: 24076680]

[22]. Srinivasan VJ, Radhakrishnan H, Lo EH, Mandeville ET, Jiang JY, Barry S and Cable AE 2012 10 methods for capillary velocimetry Biomed. Opt. Express 3 612–29 [PubMed: 22435106]

[23]. Agnew WF, McCreery DB, Yuen TG and Bullara LA 1989 Histologic and physiologic evaluation of electrically stimulated peripheral nerve: considerations for the selection of parameters Ann. Biomed. Eng 17 39–60 [PubMed: 2537589]

[24]. Shannon RV 1992 A model of safe levels for electrical stimulation IEEE Trans. Biomed. Eng 39 424–6 [PubMed: 1592409]

[25]. Demsar J et al. 2013 Orange: data mining toolbox in python J. Mach. Learn. Res 14 2349–53

[26]. Bain JR, Mackinnon SE and Hunter DA 1989 Functional evaluation of complete sciatic, peroneal, and posterior tibial nerve lesions in the rat Plast. Reconstr. Surg 83 129–38 [PubMed: 2909054]

[27]. Hammer DX, Lozzi A, Boretsky A and Welle CG 2016 Acute insertion effects of penetrating cortical microelectrodes imaged with quantitative optical coherence angiography Neurophotonics 3 025002

[28]. Bonaz B et al. 2016 Chronic vagus nerve stimulation in Crohn's disease: a 6-month follow-up pilot study Neurogastroenterol. Motil 28 948–53 [PubMed: 26920654]

[29]. Marshall R, Taylor I, Lahr C, Abell TL, Espinoza I, Gupta NK and Gomez CR 2015 Bioelectrical stimulation for the reduction of inflammation in inflammatory bowel disease Clin. Med. Insights Gastroenterol 8 55–9 [PubMed: 26692766]

[30]. Graczyk EL, Schiefer MA, Saal HP, Delhaye BP, Bensmaia SJ and Tyler DJ 2016 The neural basis of perceived intensity in natural and artificial touch Sci. Transl. Med 8 362ra142

[31]. Graczyk EL, Resnik L, Schiefer MA, Schmitt MS and Tyler DJ 2018 Home use of a neural-connected sensory prosthesis provides the functional and psychosocial experience of having a hand again Sci. Rep 8 9866 [PubMed: 29959334]

[32]. Davis TS, Wark HA, Hutchinson DT, Warren DJ, O'Neill K, Scheinblum T, Clark GA, Normann RA and Greger B 2016 Restoring motor control and sensory feedback in people with upper extremity amputations using arrays of 96 microelectrodes implanted in the median and ulnar nerves J. Neural Eng 13 036001 [PubMed: 27001946]

[33]. Chang J and Paydarfar D 2019 Optimizing stimulus waveforms for electroceuticals Biol. Cybern 113 191–9 [PubMed: 30099589]

[34]. Fisher LE, Anderson JS, Tyler DJ and Triolo RJ 2011 Optimization of stimulus parameters for selective peripheral nerve stimulation with multi-contact electrodes Conf. Proc. IEEE Engineering in Medicine and Biology Society vol 2011 pp 3039–42

[35]. McCreery DB, Agnew WF, Yuen TG and Bullara LA 1992 Damage in peripheral nerve from continuous electrical stimulation: comparison of two stimulus waveforms Med. Biol. Eng. Comput 30 109–14 [PubMed: 1640742]

[36]. Nam AS. et al. 2018; Wide-field functional microscopy of peripheral nerve injury and regeneration. Sci. Rep. 8:14004. [PubMed: 30228335]

[37]. Nepomuceno AC, Politani EL, Silva EG, Salomone R, Longo MV, Salles AG, Faria JC and Gemperli R 2016 Tibial and fibular nerves evaluation using intraoperative electromyography in rats Acta Cir. Bras 31 542–8 [PubMed: 27579882]

[38]. Haninec P 1986 Undulating course of nerve fibres and bands of Fontana in peripheral nerves of the rat Anat. Embryol 174 407–11 [PubMed: 3766995]

[39]. Islam MS, Oliveira MC, Wang Y, Henry FP, Randolph MA, Park BH and de Boer JF 2012 Extracting structural features of rat sciatic nerve using polarization-sensitive spectral domain optical coherence tomography J. Biomed. Opt 17 056012 [PubMed: 22612135]

[40]. Hunter DA, Moradzadeh A, Whitlock EL, Brenner MJ, Myckatyn TM, Wei CH, Tung TH and Mackinnon SE 2007 Binary imaging analysis for comprehensive quantitative histomorphometry of peripheral nerve J. Neurosci. Methods 166 116–24 [PubMed: 17675163]

[41]. Zochodne DW 2018 Local blood flow in peripheral nerves and their ganglia: resurrecting key ideas around its measurement and significance Muscle Nerve 57 884–95 [PubMed: 29211922]

[42]. Lim TK, Shi XQ, Johnson JM, Rone MB, Antel JP, David S and Zhang J 2015 Peripheral nerve injury induces persistent vascular dysfunction and endoneurial hypoxia, contributing to the genesis of neuropathic pain J. Neurosci 35 3346–59 [PubMed: 25716835]

[43]. Varejao AS, Meek MF, Ferreira AJ, Patricio JA and Cabrita AM 2001 Functional evaluation of peripheral nerve regeneration in the rat: walking track analysis J. Neurosci. Methods 108 1–9 [PubMed: 11459612]

[44]. Pitcher GM, Ritchie J and Henry JL 1999 Paw withdrawal threshold in the von Frey hair test is influenced by the surface on which the rat stands J. Neurosci. Methods 87 185–93 [PubMed: 11230815]

[45]. Menorca RM, Fussell TS and Elfar JC 2013 Nerve physiology: mechanisms of injury and recovery Hand Clin 29 317–30 [PubMed: 23895713]

[46]. Kawamura DH, Johnson PJ, Moore AM, Magill CK, Hunter DA, Ray WZ, Tung TH and Mackinnon SE 2010 Matching of motor-sensory modality in the rodent femoral nerve model shows no enhanced effect on peripheral nerve regeneration Exp. Neurol 223 496–504 [PubMed: 20122927]

[47]. Sato A, Sato Y and Uchida S 1994 Blood flow in the sciatic nerve is regulated by vasoconstrictive and vasodilative nerve fibers originating from the ventral and dorsal roots of the spinal nerves Neurosci. Res 21 125–33 [PubMed: 7724063]

[48]. Cha J, Broch A, Mudge S, Kim K, Namgoong JM, Oh E and Kim P 2018 Real-time, label-free, intraoperative visualization of peripheral nerves and micro-vasculatures using multimodal optical imaging techniques Biomed. Opt. Express 9 1097–110 [PubMed: 29541506]

[49]. Gora MJ, Sauk JS, Carruth RW, Lu W, Carlton DT, Soomro A, Rosenberg M, Nishioka NS and Tearney GJ 2013 Imaging the upper gastrointestinal tract in unsedated patients using tethered capsule endomicroscopy Gastroenterology 145 723–5 [PubMed: 23932950]

[50]. Parker JG et al. 2018 Diametric neural ensemble dynamics in Parkinsonian and dyskinetic states Nature 557 177–82 [PubMed: 29720658]
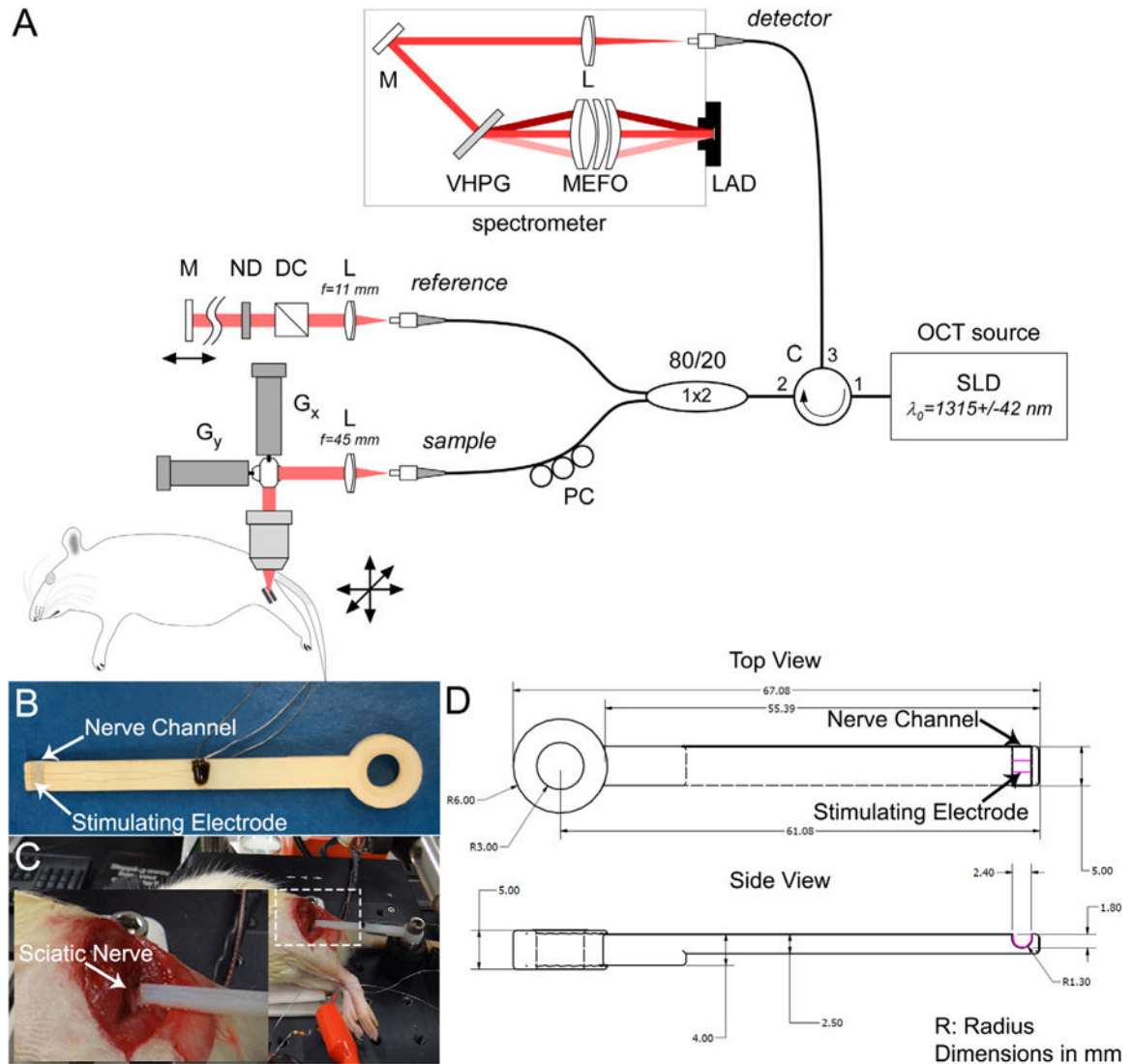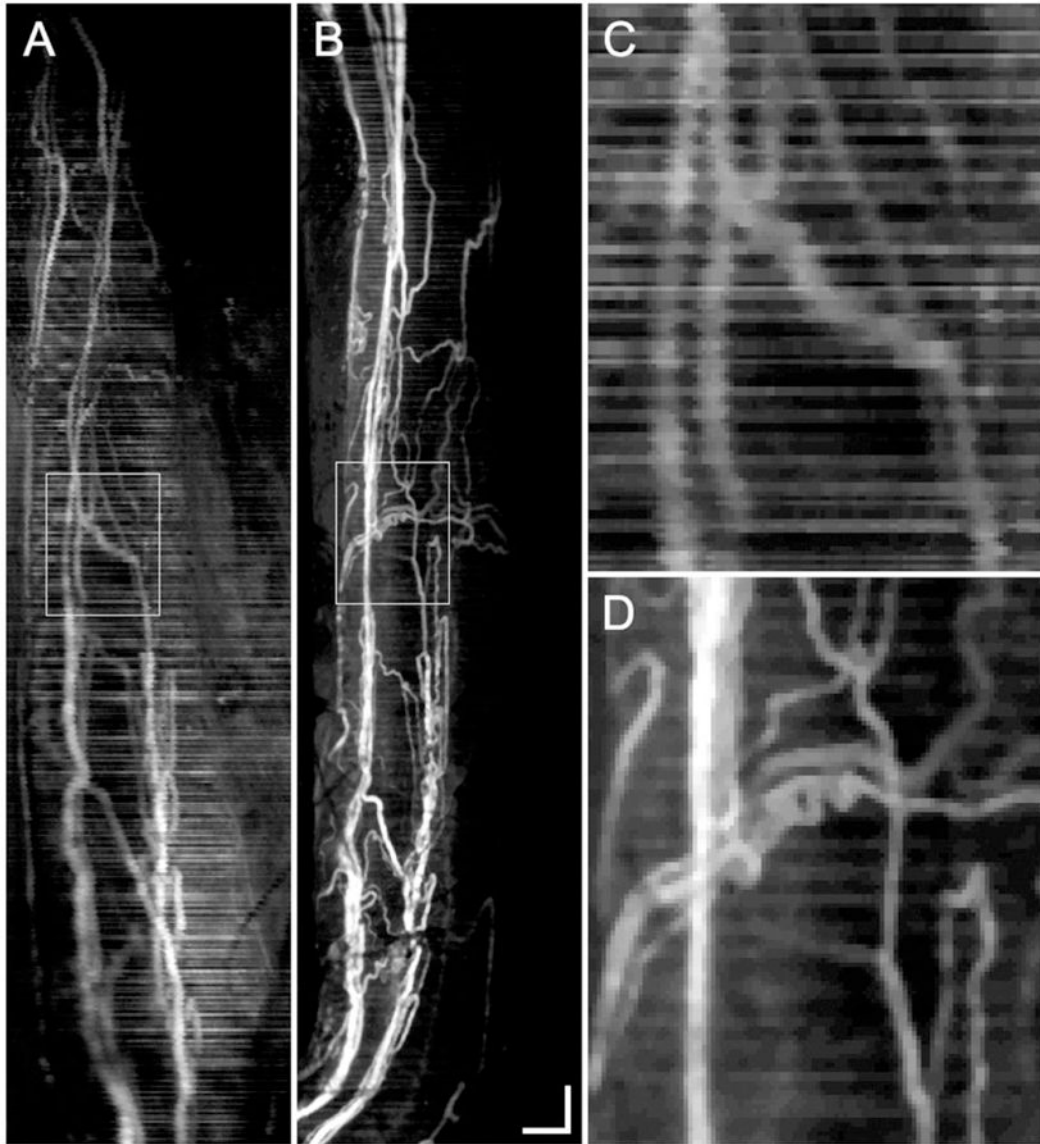
Figure 1.
OCT-A system setup used for sciatic nerve imaging. (A) Schematic of the OCT-A system. L: lens, M: mirror, VHPG: volume holographic phase grating, MEFO: multi-element focusing objective, LAD: linear array detector, SLD: superluminescent diode, C: circulator, DC: dispersion compensation cube, ND: neutral density filter, PC: polarization controller, Gx,y: galvanometers. (B) Top view of the 3D printed sNS device used for nerve stabilization, with stimulating electrodes embedded inside the nerve channel. The hemi-cuff design of the sNS forms a channel for nerve alignment and provides optical access for imaging. (C) Placement of animal on a 3-axis motorized stage for imaging. The left sciatic nerve is stabilized inside the nerve channel as shown in the inset. The sNS device is attached to the stage for stability. (D) Detailed schematic of the sNS device with dimensions.
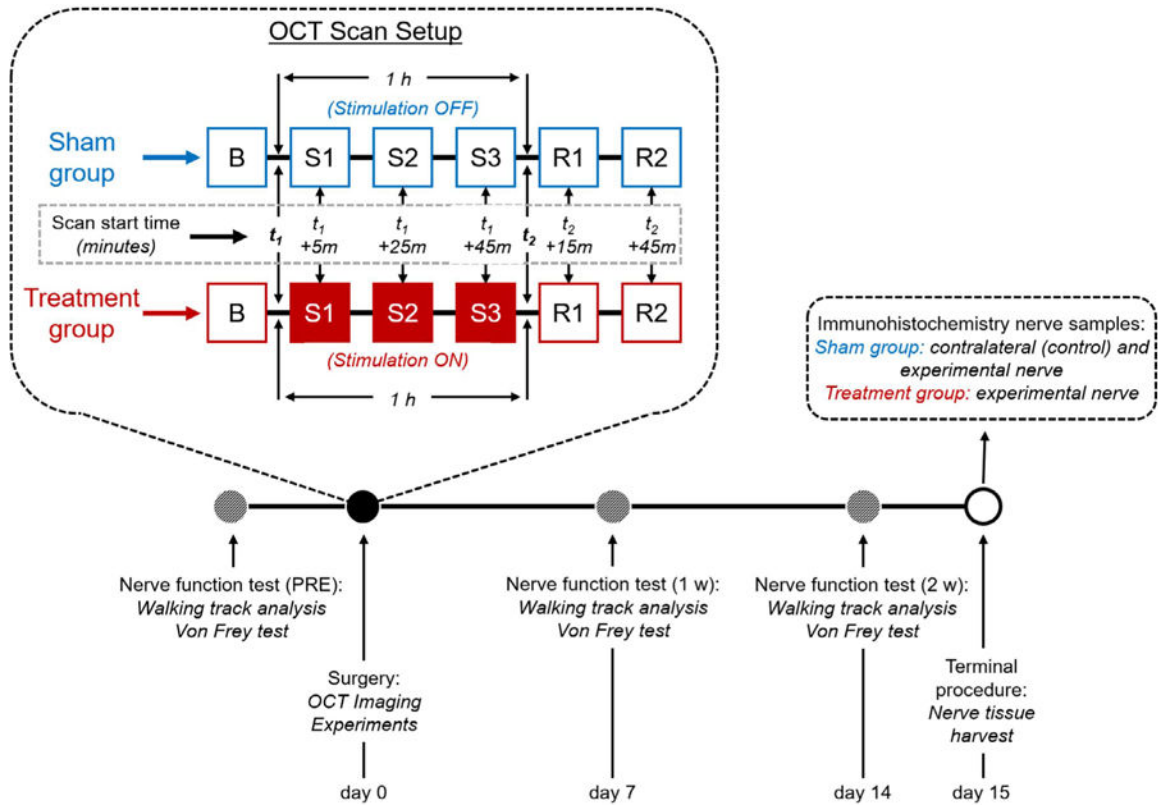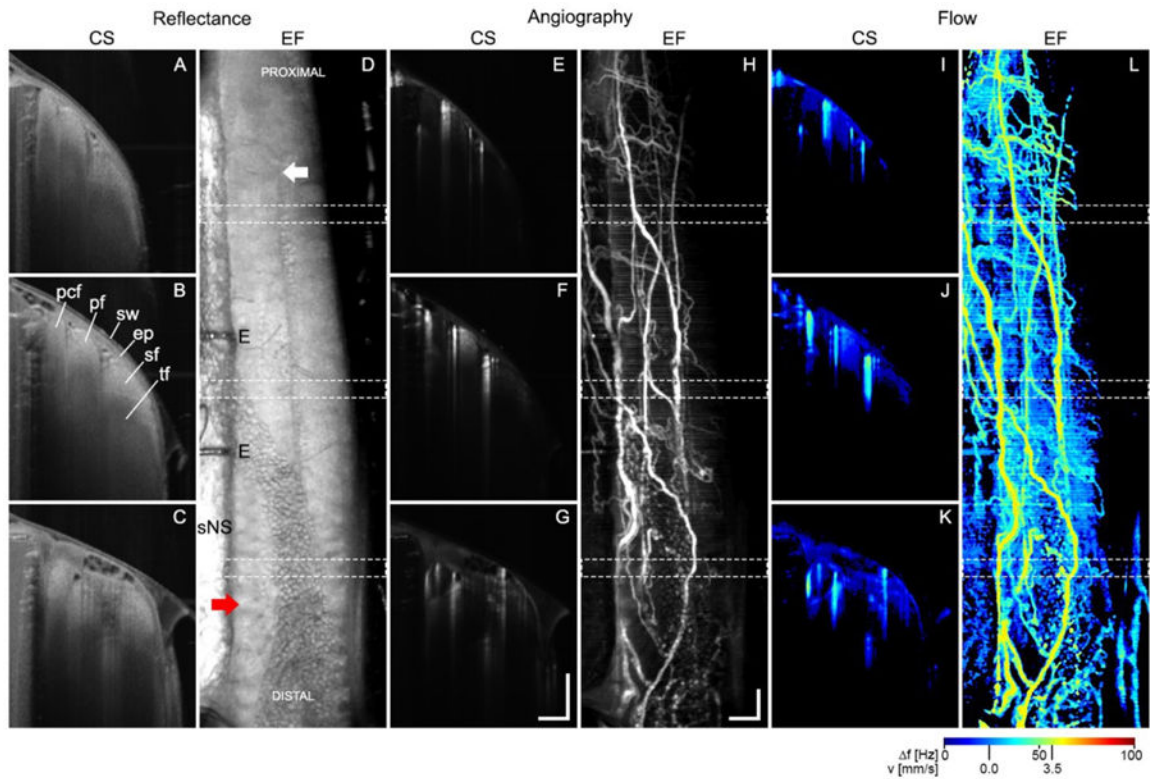
Figure 2.
Schematic representation of the experimental Protocol. Timeline for nerve function tests, surgery, and terminal procedures. OCT scan setup showing matched image scan start time for both sham and treatment groups. Stimulation was applied for 1 h only in the treatment group. t1: stimulation start, t2: stimulation stop, B: baseline scan, S1: 5 min into stimulation, S2: 25 min into stimulation, S3: 45 min into stimulation, R1: 15 min after stimulation cessation, R2: 45 min after stimulation cessation.

Figure 3.
Motion stabilization. Example *en-face* (EF) OCT images obtained (A) without and (B) with the sNS. (C) and (D) are 4 × zoomed images from the ROI delineated by the boxes shown in (A) and (B). Scalebar = 0.25 mm.
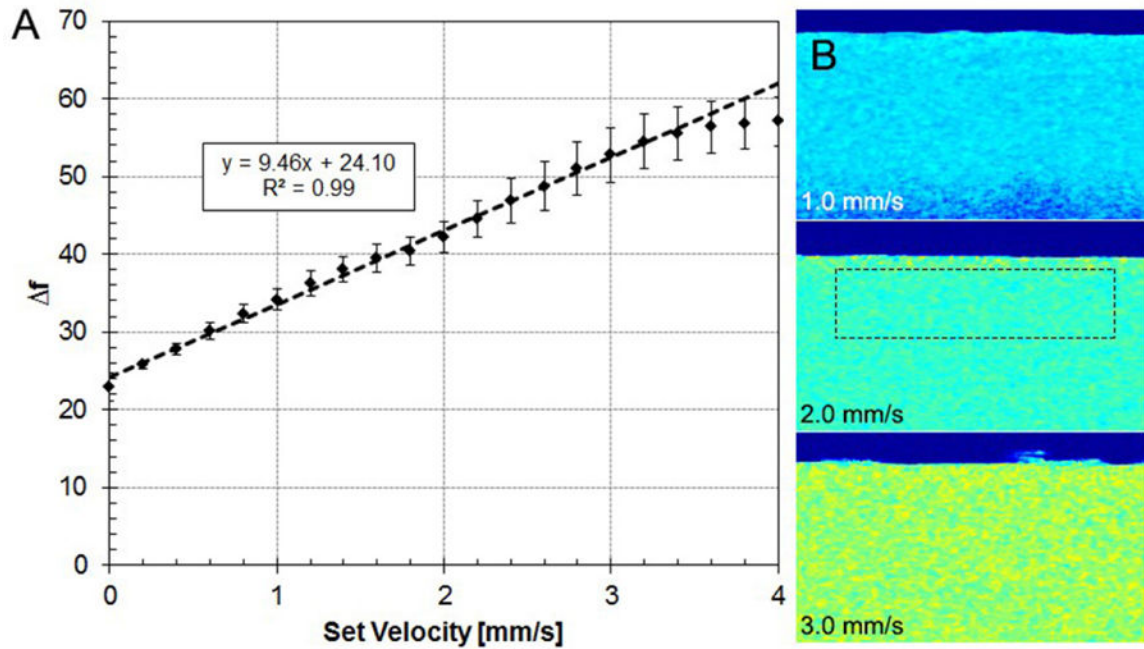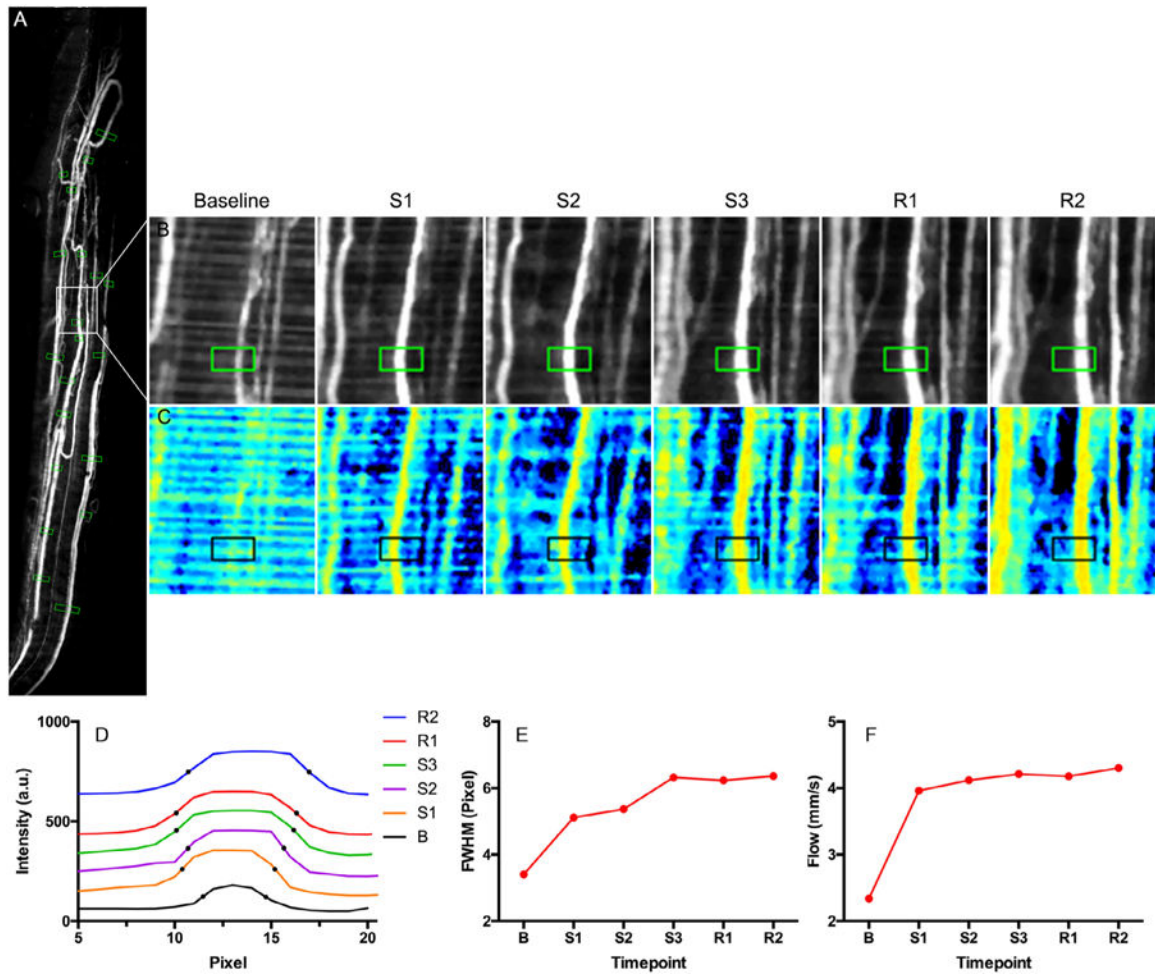
Figure 4.
Example cross-section (CS) and *en-face* (EF) reflectance, angiography and flow images of a rat sciatic nerve. (A)-(C) CS reflectance images at three points along the nerve (delineated by the dashed region in the respective EF images). (D) EF AIP reflectance image of the entire nerve channel. White arrow points to nerve bifurcation and red arrow points to bands of Fontana. Nerve structures, including the epineurium and fascicles can be identified in the CS view, while nerve bifurcation can be seen in both CS and EF views. (E)-(G) CS and (H) EF AIP angiography images of the same regions. OCT-A separates the dynamic signal from flowing blood in the vessels from the static parenchymal reflectance. (I)-(K) CS and (J) EF MIP capillary flow images. Color bar indicates corresponding flow velocities. ep: epineurium; sw: Saranwrap, pcf: peroneal cutaneous fascicle, pf: peroneal fascicle, sf: sural fascicle, tf: tibial fascicle, sNS: stimulating nerve stabilizer, E: electrode. Scalebars = 0.25 mm.
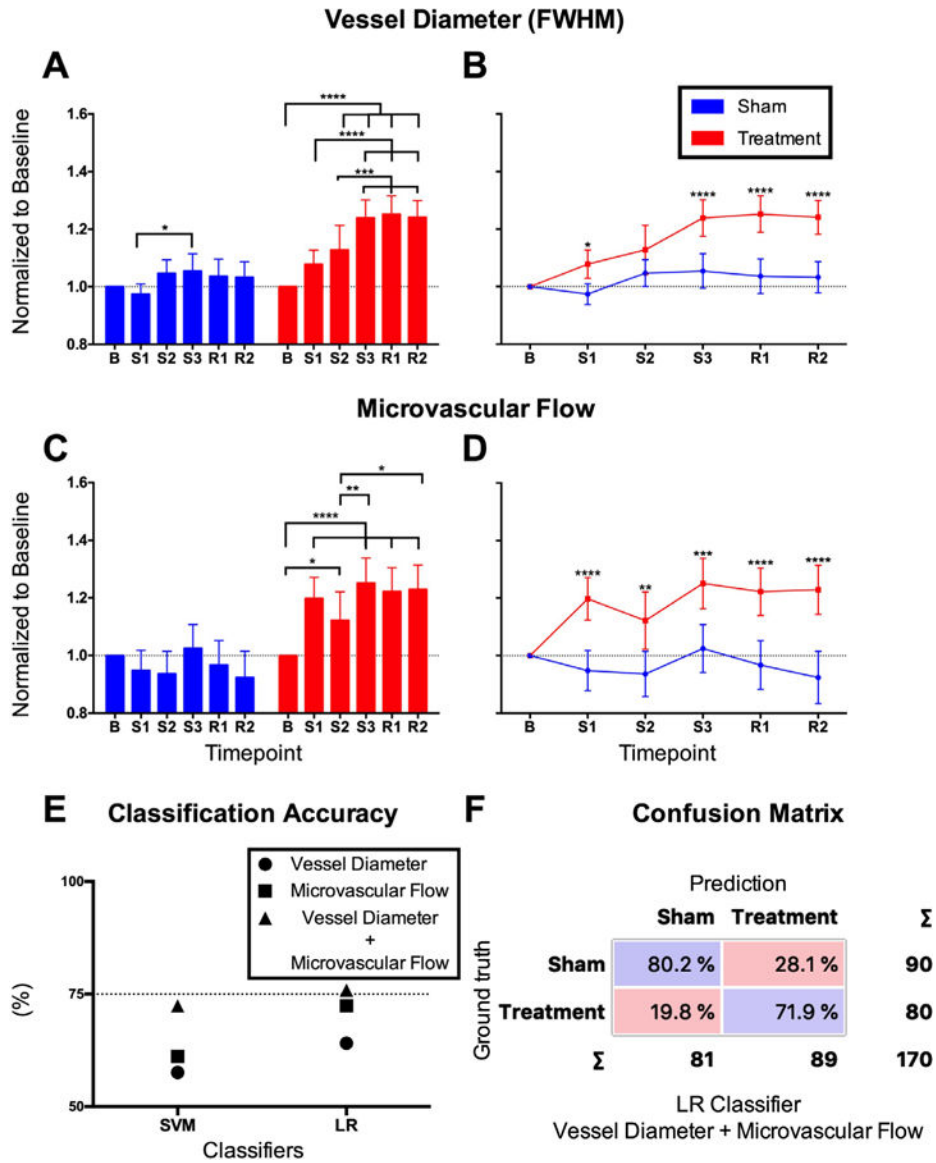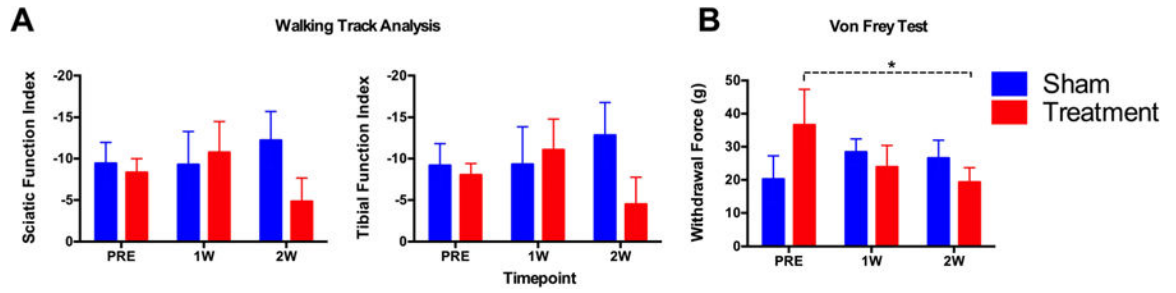
Figure 5.
Flow calibration. OCT-A capillary flowmetry calibration was accomplished with a uniform scattering phantom. (A) The linear relationship between frequency bandwidth (*f*) and flow velocity is plotted, where each data point is the mean SD *f* value calculated from a 50 200 pixel region-of-interest shown in (B), acquired with the phantom moving at a fixed velocity on a precision linear stage. (B) Three OCT-A flowmetry images across the range are shown for example.

Figure 6.
Vessel diameter and flow measurements. Example of vasodilation and increased flow during stimulation. (A) EF AIP angiography image of a treatment nerve. (B) Angiography maps of the boxed region in (A) at baseline and timepoints S1, S2, S3, R1, and R2. Green boxes indicate vessel segments used for analysis. (C) Flow maps of same region with black boxes indicating same analysis regions. (D) Vessel profiles for the six timepoints for a single region (green box in (B)) indicating dilation during stimulation. (E) FWHM vessel diameter extracted from profiles in (D). (F) Peak flow measurement (mm/s) for the same vessel segment.
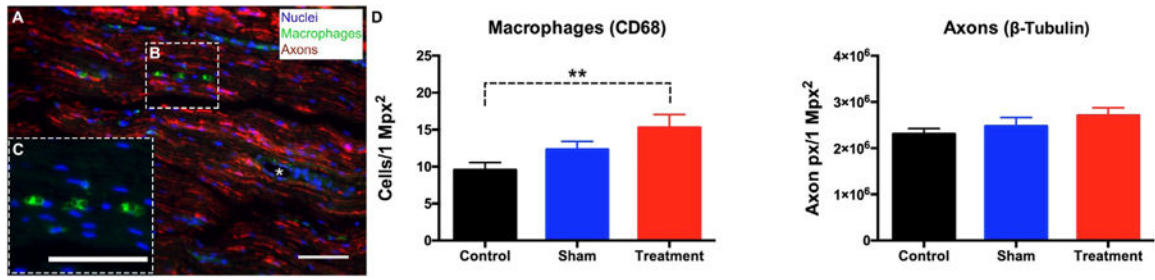
Figure 7.
Vessel diameter and microvascular flow measurements. (A) Within group comparison of normalized vessel diameter, with each data point representing average of all vessels from all animals in the group. (B) Comparison of vessel diameter between sham and treatment groups at each time point. (C) Within group comparison of normalized microvascular flow, with each data point representing average of all vessels from all animals in the group. (D) Comparison of microvascular flow between sham and treatment groups at each time point. (E) Comparison of SVM and LR classifiers with data showing improved average classification accuracy when features from both vessel diameter and microvascular flow are used. (F) Confusion matrix of LR classification showing prediction accuracy using both vessel diameter and microvascular flow features. Data in (A)-(D) shown as Mean 95% confidence interval. Statistical difference *p ≤ 0.05, **p ≤ 0.01, ***p ≤ 0.001, and ****p ≤ 0.0001.

Figure 8.
Assessment of functional changes. (A) Walking track analysis was used to compute the SFI and TFI. Compared to pre-stimulation (PRE), a decrease in SFI and TFI indicates loss of function. There was no significant loss in motor function compared to PRE. (B) Von Frey test was used to assess mechanical allodynia. Hypersensitivity in response to mechanical force was observed in the treatment group at two weeks compared to PRE. Data on the graph shown as Mean ± S.E. Statistical difference *$p \leq 0.05$.

Figure 9.
Nerve tissue response to electrical stimulation. (A) Nerve sections were stained for axons (red), CD68+ macrophages (green), and nuclei (blue). Presence of blood vessels inside the nerve is indicated by asterisk. (C) Inset showing CD68+ cells in region (B) without the axon layer. (D) Comparison of the number of CD68+ cells and axon pixels between groups. Only the CD68+ cells are significantly higher in the treatment group compared to control. Scalebar = 100 μm. Data shown as mean ± S.E. Statistical difference **$p \leq 0.01$.